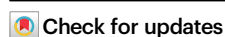


Oxygen-doped carbon-supported palladium nanoparticles boost the tandem hydrogenation–acetalization–hydrogenolysis of phenols and diphenyl ethers to cyclohexyl ethers

Received: 19 December 2024

Accepted: 19 May 2025

Published online: 29 May 2025

Lang Jiang^{1,5}, Xiang Li^{2,5}, Yiqian Ma¹, Yiliang Hua³, Yicheng Peng¹, Mengxiang Ma¹, Chengxiang Shi⁴, Jun Wang¹, Ji-Jun Zou⁴ & Qiang Deng¹✉

The one-pot hydrotreatment of phenols to cyclohexyl ethers is crucial but difficult to achieve for fine chemical synthesis owing to the easy overhydrogenation to cyclohexanols over traditional metal–acid bifunctional catalysts. Herein, surface oxygen-doped carbon-supported Pd nanoparticles (Pd/C-O) were prepared via nitric acid oxidation and subsequent incipient wetness impregnation, demonstrating the tandem hydrogenation–acetalization–hydrogenolysis route of phenol to cyclohexyl methyl ether, achieving a significant yield of 97.9% in a methanol solvent at a low temperature of 110 °C. Catalytic mechanism investigation indicated that the in situ hydrogen spillover from Pd nanoparticles to the Pd–O–C interface formed H^+-H^- pairs, which acted as uncommon active sites for hydrogenation and hydrogenolysis steps and also provided Brønsted acid sites for the acetalization step, thereby triggering the facile preparation of cyclohexyl methyl ether. Furthermore, the prepared catalyst exhibited excellent catalytic generality for synthesizing cyclohexyl ethers from various phenols or alcohol solvents via a similar reaction route and great expansibility from diphenyl ethers via preliminary partial hydrogenation–alcoholysis steps. The study reports an interesting bifunctional catalysis for challenging tandem reaction routes toward cyclohexyl ether synthesis by harnessing an oxygen-doped carbon support to form transient H^+-H^- pairs.

Cyclohexyl methyl ether (CME) has great prospects in industrial manufacturing because it can replace petroleum-based cyclopentyl methyl ether as an aliphatic ether solvent in various applications, including organic chemistry and lithium battery industries^{1–3}. In

addition, owing to its high octane number and high boiling point, it can also be used as a potential fuel⁴. At present, the main synthetic route of CME is based on the hydrogenation of phenyl methyl ether and the etherification of cyclohexanol with methanol^{5,6}. Lignin, a sustainable

¹School of Chemistry and Chemical Engineering, Nanchang University, No. 999 Xuefu Avenue, Nanchang, P. R. China. ²College of Forestry, Jiangxi Agricultural University, No. 1101 Zhimin Avenue, Nanchang, P. R. China. ³School of Future Technology, Nanchang University, No. 999 Xuefu Avenue, Nanchang, P. R. China. ⁴School of Chemical Engineering and Technology, Tianjin University, Tianjin, P. R. China. ⁵These authors contributed equally: Lang Jiang, Xiang Li.

✉ e-mail: dengqiang@ncu.edu.cn

carbon source, contains abundant aromatic structural units and can be easily transformed into several important platform molecules, such as phenol monomers and diphenyl ether dimers⁷. The conversion of these model compounds into cyclohexyl ethers is an excellent entry point for biomass refining^{8–10}.

Theoretically, CME can be prepared from phenol via a two-step methylation–hydrogenation method including the *O*-methylation of phenol with methanol to phenyl methyl ether with a yield of 40%–90% at 270–400 °C over solid acids (e.g., ZSM-5/MCM-41, LaPO₄/SBA-15, H-mordenite, AlCl₃, and FeCl₃)^{11–14}, followed by the hydrogenation of phenyl methyl ether to CME with a yield of 50%–90% over metal-based catalysts (e.g., Ru/C, Ru@ITQ, Ru/SiO₂-SO₃H, Ru/Al₂O₃, and Pt/Al₂O₃) at 30–170 °C^{5,15–17}. However, these two-step reaction systems require harsh reaction temperatures in the etherification step, prolonged reaction times, and an additional isolation step for phenyl methyl ether intermediates. Considering the general trend toward the green chemistry industry, the one-pot direct phenol conversion of phenol to CME is highly desirable. Several metal–solid acid bifunctional catalysts, including physical mixtures of metals and acids (e.g., Raney Ni + SAPO-11 and Pd/C + HZSM-5)^{18,19} and metal-supported solid acids (e.g., Ni/Al₂O₃, Rh/ZrH₂(PO₄)₂, and Ru/CoO) have been explored for the hydrotreatment of phenol in a methanol solvent^{20–22}. However, cyclohexanol is a common product and target CME is scarcely produced. To the best of our knowledge, only one study has been reported CME synthesis at a high temperature of 200 °C using a mixture of Pd/C and HZSM-5 as a catalyst by delicately coordinating the amounts of metal and acidic sites. This reaction involved the initial metal-catalyzed hydrogenation of phenol to cyclohexanone, acid-catalyzed acetalization to cyclohexanone dimethyl acetal, followed by bifunctional sites-catalyzed hydrogenolysis¹⁹. Unfortunately, current catalytic results are still unsatisfactory. First, while precious metal-based catalysts exhibit rapid hydrogenation activity owing to their strong H₂ activation ability, overhydrogenated cyclohexanol is easily formed due to further C = O hydrogenation, which cannot be etherified to afford the target CME^{18–22}. Second, because bifunctional sites over mixed catalysts are separated, the long-range diffusion of intermediates, such as cyclohexanone from metal to acidic sites, leads to an inferior synergy. It tends to hydrogenate over metal sites rather than undergo acetalization over acid sites, which further causes low CME selectivity. Third, currently, the main reactant and solvent used in the reaction are phenol and methanol, and phenol-based derivatives (e.g., 4-methylphenol, 2-methoxyphenol, and 3-methoxyphenol) and methanol homologs (e.g., ethanol, isopropanol, and *sec*-butanol) have scarcely been investigated. Therefore, developing bifunctional catalysts with adjacent metal–acid sites is crucial to promote the cascade conversion of phenols to cyclohexyl ethers, particularly maintaining an excellent catalytic generality under mild reaction conditions.

Herein, O-doped carbon-supported Pd nanoparticles were fabricated via a nitric acid (HNO₃) oxidation and subsequent incipient wetness impregnation method for the hydrogenation–acetalization–hydrogenolysis of phenol in a methanol solvent. Results show that H₂ is activated on Pd nanoparticles to form H atoms, which migrates to the adjacent O atom on the carbon support to form H⁺–O[–]–Pd–H⁺. The in situ generated H⁺–H⁺ pair not only acts as active sites for phenol hydrogenation and cyclohexanone dimethyl acetal intermediate hydrogenolysis steps but also acts as Brønsted acid sites for the acetalization step of cyclohexanone with methanol. Notably, cyclohexanone formed on hydrogenation sites rapidly transfers to Brønsted acid sites for the acetalization steps, avoiding long-range diffusion. Consequently, Pd/C–O catalysts simultaneously exhibit high activity and superior selectivity with a significant CME yield of 97.9% from phenol at a low temperature of 110 °C. This low-temperature hydrogenation–acetalization–hydrogenolysis process shows broad applicability for various phenols (e.g., 2-methoxyphenol, 3-methoxyphenol, 4-methylphenol, and 2-methoxy-4-formyl phenol) and

alcohols (i.e., ethanol, isopropanol, and *sec*-butanol). Furthermore, some diphenyl ethers (e.g., diphenyl ether, 4,4′-dimethyl diphenyl ether, 4-methylphenyl phenyl ether, and 3-methylphenyl phenyl ether) and phenyl ethers (i.e., benzyl phenyl ether and 2-phenylethyl phenyl ether) afford high cyclohexyl ether yields, except additional partial hydrogenation–alcoholysis steps to cyclohexanones and phenols are required. This study reports a tandem hydrogenation–acetalization–hydrogenolysis route of phenols with notable flexibility for tuning cyclohexyl ether specifications over in situ generated H⁺–H⁺ pairs via the hydrogen spillover mechanism on the Pd/C–O catalyst.

Results

Structural characteristics of catalysts

The Pd/C–O catalyst was prepared via an HNO₃ treatment method using commercial activated carbon (C) in a 20.0 wt% HNO₃ solution. Next, the O-doped carbon (C–O) was used as the support for incipient impregnation using palladium chloride (PdCl₂) as the Pd precursor, followed by sodium borohydride (NaBH₄) reduction (Fig. 1a). For comparison, C-supported Pd without O doping (Pd/C) was prepared via a similar method except without the HNO₃ treatment step. The powder X-ray diffraction (XRD) patterns showed the peaks of the amorphous carbon support and a distinct (111) crystal plane of Pd nanoparticles at 2θ = 40.0° (Supplementary Fig. 1a)^{23,24}. N₂ adsorption–desorption isotherms, transmission electron microscopy (TEM) images and carbon monoxide (CO) pulse purge indicated that Pd/C and Pd/C–O possessed similar textural structures with Brunauer–Emmett–Teller specific surface areas (S_{BET}) of 2144–2212 m²·g^{−1} and comparable Pd nanoparticle sizes of 1–6 nm and analogous Pd dispersity of about 40% (Supplementary Fig. 1b–e and Supplementary Table 1). The high-angle annular dark-field scanning TEM (HAADF–STEM) image showed a lattice spacing of 0.220 nm, which is in agreement with the standard Pd (111) plane (Fig. 1b)^{23,24}. Meanwhile, the dispersive X-ray spectroscopy (EDS) elemental mapping confirmed that the intimacy of the Pd and O elements (Supplementary Fig. 1f–i). Furthermore, the linear EDS analysis showed an identical trend of Pd and O signal intensities, indicating that Pd was preferentially attached to the O species instead of to the C species (Supplementary Fig. 2a). Inductively coupled plasma optical emission spectroscopy (ICP–OES) indicated 0.9–1.0 wt% Pd contents for Pd/C and Pd/C–O, whereas elemental analysis for O content largely increased from 1.7 wt% in Pd/C to 12.0 wt% in Pd/C–O, indicating the successful introduction of O-containing groups during the oxidation step (Supplementary Table 1). The Raman spectra showed D- (1324 cm^{−1} for defected carbon) and G-bands (1584 cm^{−1} for graphitic sp² carbon) (Fig. 1c)²⁵. The oxidation step decreased the degree of graphitization, as indexed by the higher peak intensity ratio of the D to G bands. Furthermore, the intensity of C = C bond peak (1359 cm^{−1}) decreased in Fourier transform infrared (FTIR) spectra. However, the intensities of the peaks at 1099, 1616, and 3419 cm^{−1}, corresponding to the stretching vibrations of C–O, C = O, and O–H bonds, respectively, were higher in the FTIR spectrum of Pd/C–O than that of Pd/C, confirming that O incorporation was successful with bonding types of O–H, C–O and C = OO– (Fig. 1d)^{25–27}.

Previous reports revealed that the OH-containing groups (C = OOH and C–OH) of the carbon support can be easily substituted with PdCl₂ to form HCl during the incipient process, and the Pd–O–C interface can be formed^{25,28,29}. Indeed, after the introduction of Pd, the O–H peak intensity of C–O drastically decreased (Supplementary Fig. 2b). The high-resolution Pd 3d X-ray photoelectron spectroscopy (XPS) spectra of Pd/C and Pd/C–O showed a metallic Pd⁰ signal (3d_{5/2} peak = 335.7 eV, 3d_{3/2} peak = 340.9 eV), whereas the Pd 3d XPS spectrum of Pd/C–O was dominated by the oxidative Pd²⁺ signal (3d_{5/2} peak = 337.9 eV, 3d_{3/2} peak = 342.9 eV) (Fig. 1e)^{23,24}. In addition, the O 1s spectra exhibited C = O (532.1 eV), C–O (533.2 eV) and O–H bonds (534.2 eV), and the C 1s spectra showed C = C (284.6 eV), C–C

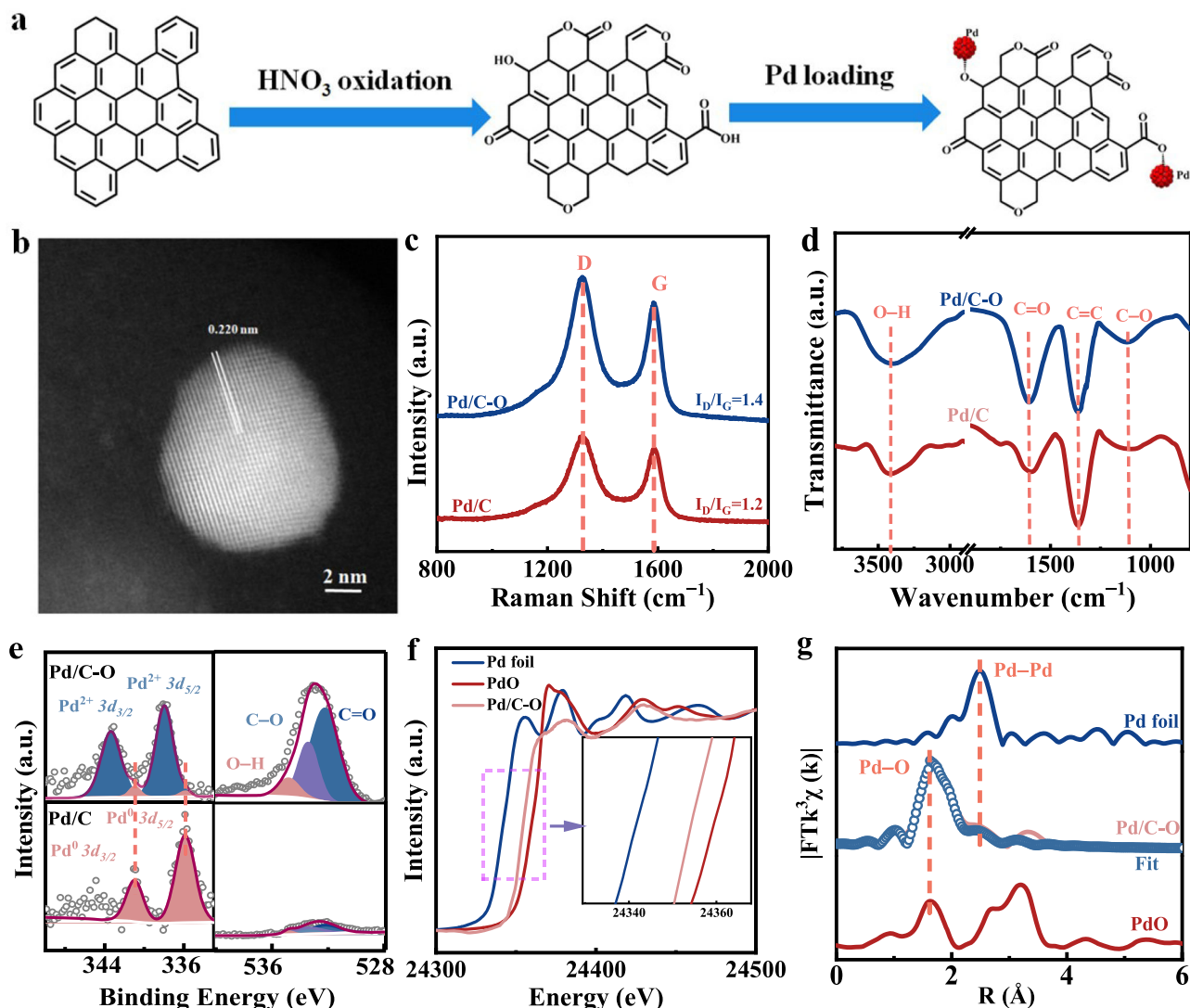


Fig. 1 | Synthesis and characterizations for Pd/C-O catalysts. **a** Synthesis of Pd/C-O, **b** TEM micrographs of Pd/C-O, **c** Raman spectra and **d** FTIR spectra of Pd/C and Pd/C-O; **e** Pd 3d and O 1s XPS spectra of Pd/C and Pd/C-O, **f** Pd K-edge XANES spectra and **g** FT-EXAFS analysis and fitting plots at *R* space of various samples.

(285.1 eV), C-O (286.0 eV), and C=O (287.9 eV) bonds (Fig. 1e and Supplementary Fig. 2c). The Pd coordination environment of Pd/C-O was further investigated using extended X-ray absorption fine-structure (EXAFS) spectroscopy, which revealed that the X-ray absorption energy of Pd/C-O was higher than that of Pd foil but lower than that of PdO (Fig. 1f). Meanwhile, the Fourier transform k^3 -weighted $\chi(k)$ EXAFS (FT-EXAFS) spectrum of Pd/C-O showed peaks corresponding to Pd-O (1.6 Å, without correction) and Pd-Pd coordinations (2.4 Å, without correction) (Fig. 1g)^{24,30–32}. Furthermore, the wavelet transform EXAFS spectrum exhibited two prominent peaks (1.8 Å, 5.2 Å⁻¹; 2.8 Å, 13.6 Å⁻¹), associated with Pd-O and Pd-Pd bonds, respectively (Supplementary Fig. 2d). The quantitative EXAFS fitting results of the Pd/C-O in *k* and *R* spaces indicated that the average coordination numbers of Pd-O and Pd-Pd were approximately 5.3 and 10.8, respectively (Fig. 1g and Supplementary Fig. 2e, Supplementary Table 2). These results demonstrated that Pd nanoparticles were supported on carbon with an abundant Pd-O-C interface.

Hydrogenation-acetalization-hydrogenolysis of phenols

The catalytic performance of Pd/C-O was evaluated in the phenol (PHO) reaction at 110 °C in a methanol solvent using Pd/C (with the same Pd content) and commercial Ru/C as references. The carbon

balance was >97% under the reaction conditions. As shown in the time-dependent product distributions, Pd/C, Ru/C, and Pd/C-O exhibited strikingly different catalytic behaviors. First, Ru/C showed 88.6% conversion of PHO after 6 h, but only overhydrogenated cyclohexanol (CHL) was obtained via the PHO hydrogenation to cyclohexanone (CHO) and subsequent C=O hydrogenation route (Fig. 2a, b). This catalytic performance is expected because carbon is viewed as an inert support during bifunctional catalysis. The intermediates and products were verified via gas chromatography-mass spectrometry (Supplementary Fig. 3a–f). Pd/C was almost inactive, and no obvious products were detected (Supplementary Fig. 3g). By contrast, Pd/C-O showed an interesting hydrogenation-acetalization-hydrogenolysis route involving the initial hydrogenation to CHO, semi-acetalization 1-methoxycyclohexanol (MCHL), acetalization to 1,1-dimethoxycyclohexane (DMC), followed by hydrogenolysis to CME with a conversion of 97.0% and selectivity of 90.8%. Correspondingly, the parallel overhydrogenation route was completely avoided, as evidenced by the near-zero selectivity toward CHL (1.6%) (Fig. 2c). Control experiments over Pd/C-O showed the inactivity of CHL feedstock, further confirming the hydrogenation-acetalization-hydrogenolysis route for CME synthesis (Supplementary Fig. 3h). Trace amount of MCHL was observed in the time-dependent product distribution, proving

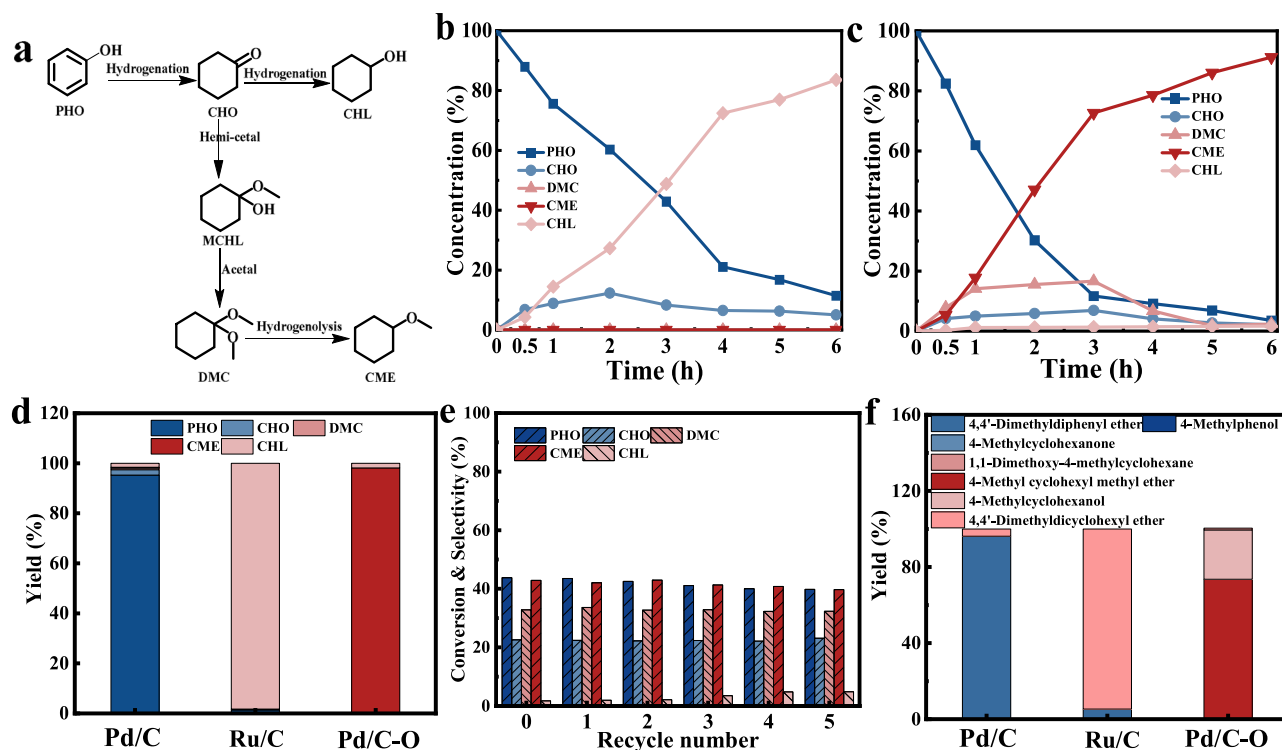


Fig. 2 | Catalytic performance, reaction pathways, and recyclability of catalysts in phenol etherification reactions. **a** Reaction pathway and time-dependent product distribution of PHO reaction over **b** Ru/C and **c** Pd/C-O; **d** Catalytic performance of various catalysts in PHO reaction; **e** recycled performance of Pd/C-O in PHO reactions; **f** catalytic performance of various catalysts in 4,4'-dimethyl diphenyl ether reaction. Reaction conditions: methanol (15 mL), temperature

(110 °C), H₂ (2.0 MPa), **b** PHO (0.09 mmol), Ru/C (2 mg), **c** Pd/C-O (20 mg), PHO (0.09 mmol), **d** PHO (0.09 mmol), time (12 h), Ru/C (2 mg), Pd/C (20 mg), or Pd/C-O (20 mg); **e** PHO (0.09 mmol), Pd/C-O (20 mg), time (1 h). **f** 4,4'-Dimethyl diphenyl ether (0.09 mmol), Ru/C (5 mg), Pd/C (50 mg), Pd/C-O (50 mg), time (12 h). The products were quantified by GC.

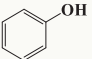
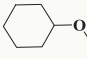
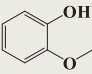
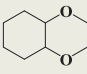
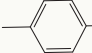
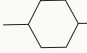
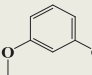
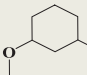
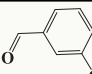
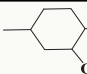
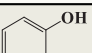
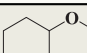
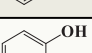
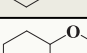
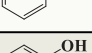
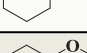
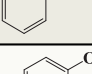
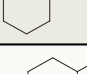
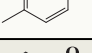
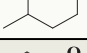
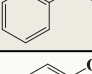
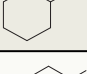
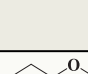
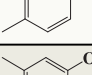

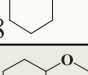
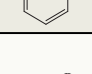
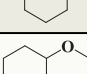
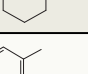
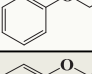
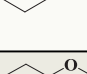
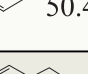
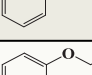
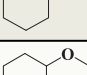
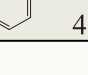
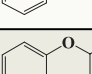
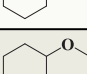
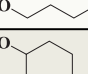
considerably slow reaction rates for PHO hydrogenation, CHO acetalization, and DMC hydrogenolysis steps in the catalytic process. After 12 h, PHO is completely converted with a CME selectivity of up to 97.9% over Pd/C-O (Table 1 entry 1). Notably, even though the hydrotreatment of PHO has been widely reported over various bifunctional catalysts in a methanol solvent, Pd/C-O is the catalyst that pioneers the use of the hydrogenation–acetalization–hydrogenolysis route for selective CME synthesis, which was previously unattainable over conventional catalysts, including nonprecious metal catalysts (e.g., Raney Ni + SAPO-11, Ni/Al₂O₃, and Co-Ni@NC) and precious metal catalysts (e.g., Rh/ZrH₂(PO₄)₂, Ru/CoO, Ru-NC/SiO₂-Al₂O₃, Pd/C + HZSM-5, Pd/C, and Pd/NC)^{18–22,33–37} (Supplementary Table 3). These catalysts often show an overhydrogenation route for CHL synthesis due to the long-range diffusion of CHO intermediate.

Subsequently, the reactant amount and reaction temperature were optimized. As the PHO amount gradually increased from 0.09 mmol to 0.90 mmol, PHO conversion and CME selectivity decreased from 99.9% and 97.9% to 9.7% and 36.7%, respectively, after 12 h (Supplementary Fig. 4a). Fortunately, Pd/C-O exhibited astonishing activity (95.4%) and selectivity (94.6%) when the reaction temperature increased to 170 °C (Supplementary Fig. 4b). A hot filtration experiment showed no further PHO conversion and CME generation in the filtrate, demonstrating almost no leaching of Pd metal (Supplementary Fig. 4c). After the catalytic process, the spent Pd/C-O was obtained by centrifugation, washed with methanol and water, and dried under a vacuum, and exhibited a stable PHO activity and CME selectivity for five runs (Fig. 2e). XRD, TEM, ICP-OES, and XPS analyses further confirmed the robust physicochemical properties of Pd/C-O during catalytic reactions (Supplementary Fig. 4d–h and Supplementary Table 4). In addition, the Pd/C-O also showed a great catalytic performance in a fixed-bed reactor with the PHO

conversion and CME selectivity both above 93.0% in 10 h (Supplementary Fig. 4i).

Next, the catalytic performance of Pd/C-O was investigated for other phenols. 2-Methoxyphenol (named guaiacol), is the most common component of lignin oil; it afforded the corresponding 2-methoxy cyclohexyl methyl ether via a similar route, as indexed by the time-dependent product distribution (Supplementary Fig. 5a, b)^{37,38}. Pd/C-O simultaneously exhibited high guaiacol conversion (99.9%) and great 2-methoxy cyclohexyl methyl ether selectivity (73.4%) after 12 h (Table 1 entry 2). Similarly, various phenols (e.g., 4-methylphenol and 3-methoxyphenol) exhibited the same hydrogenation–acetalization–hydrogenolysis performance in terms of synthesizing the corresponding cyclohexyl methyl ethers (i.e., 4-methyl cyclohexyl methyl ether and 3-methoxy cyclohexyl methyl ether), achieving impressive yields of 91.0%–92.9% over Pd/C-O (Table 1 entries 3–4). In addition, 2-methoxy-4-formylphenol (named vanillin) showed a superior conversion rate of 99.9% and a 2-methoxy-4-methyl cyclohexyl methyl ether selectivity of 72.0% after 12 h (Supplementary Fig. 5c, d and Table 1 entry 5). The evolution of products in vanillin reaction was largely analogous to that for the guaiacol reaction, except for a common prerequisite hydrogenation–hydrogenolysis step for conversion of vanillin to 2-methoxy-4-methylphenol^{39,40}. Next, the hydrogenation–acetalization–hydrogenolysis route was further assessed in different alcohol solvents (i.e., ethanol, isopropanol, and *sec*-butanol) (Supplementary Fig. 5e–g and Table 1 entries 6–8). Similar to methanol, the corresponding cyclohexyl ethers (i.e., cyclohexyl ethyl ether, cyclohexyl isopropyl ether, and cyclohexyl *sec*-butyl ether) were selectively obtained over Pd/C-O, delivering good yields of 36.5%–89.4%. Although the hydrotreatment of these phenol derivatives has been widely reported in alcohol solvents over various catalysts (e.g., Pd/C, Ru/CoO, Rh@SiO₂, Ru/hydrotalcite, Ru-NC/SiO₂-Al₂O₃, and Pd/NaY), to the best

Table 1 | Substrate scope of phenols, diphenyl ethers and phenyl ethers

Entry	Reactants	Solvent	Time (h)	Conversion (%)	Product selectivity (%)
1		Methanol	12	99.9	 97.9
2		Methanol	12	96.7	 73.4
3		Methanol	12	99.9	 91.0
4		Methanol	12	99.9	 92.9
5		Methanol	12	99.9	 72.0
6		Ethanol	12	99.9	 89.4
7		Isopropanol	12	99.9	 52.7
8		Sec-butanol	12	99.9	 36.5
9		Methanol	12	99.9	 73.5
10		Methanol	12	99.9	 51.1
11		Methanol	12	99.9	 37.8  24.8
12		Methanol	12	99.9	 34.3  26.2
13		Methanol	12	99.9	 48.5  50.4
14		Methanol	12	99.9	 41.3  47.1
15		Methanol	48	99.9	 48.1  48.3
16		Methanol	12	99.9	 41.6  48.0

Reaction conditions: reactant (0.09 mmol), Pd/C-O (0.02 g for phenols, 0.05 g for diphenyl ethers and phenyl ethers), solvent (15 mL), temperature (110 °C), and H₂ (2.0 MPa). The products were quantified by GC.

of our knowledge, the selective synthesis of cyclohexyl ethers from various phenols and alcohol solvents is rarely reported (Supplementary Table 5)^{22,34,37,39–44}.

Hydrogenation–alcoholysis of diphenyl ethers

The catalytic performance of Pd/C-O was further studied in diphenyl ether reactions. 4,4'-Dimethyl diphenyl ether, a model dimer for 4-O-5 linkages in lignin, is relatively more stable than PHO and showed a low conversion rate under identical reaction conditions (Supplementary Fig. 6a, b). Therefore, the Pd/C-O amount in the system was increased to 50 mg. It was transformed to 4-methyl cyclohexyl methyl ether via a tandem hydrogenation–alcoholysis–hydrogenation–acetalization–hydrogenolysis route, involving the initial partial hydrogenation to 4-methylphenyl-4'-methylcyclohexenyl ether, alcoholysis to

4-methylphenol + 4-methyl cyclohexyl methyl ether, and final hydrogenation–acetalization–hydrogenolysis of 4-methylphenol to 4-methyl cyclohexyl methyl ether, as shown by the time-dependent product distribution (Supplementary Fig. 6c). After 12 h, Pd/C-O still showed a 4,4'-dimethyl diphenyl ether conversion of 99.9% and a 4-methyl cyclohexyl methyl ether selectivity of 73.5% (Fig. 2f and Table 1 entry 9). In comparison, Pd/C was inactive and Ru/C afforded overhydrogenated 4,4'-dimethyl dicyclohexyl ether (Fig. 2f, Supplementary Fig. 6d, e). Meanwhile, diphenyl ether, 4-methyl diphenyl ether, and 3-methyl diphenyl ether were used in the reaction and converted into their corresponding cyclohexyl methyl ether (i.e., cyclohexyl methyl ether, cyclohexyl methyl ether + 4-methyl cyclohexyl methyl ether, and cyclohexyl methyl ether + 3-methyl cyclohexyl methyl ether, respectively) with a total cyclohexyl methyl ether

selectivity of >50% over Pd/C-O (Table 1 entries 10–12). Unlike diphenyl ether, benzyl phenyl ether (featuring an α -O-4 type dimer) and 2-phenylethyl phenyl ether (featuring a β -O-4 type dimer) underwent the initial hydrogenolysis to PHO + methylbenzene and PHO + ethylbenzene, respectively, followed by the hydrogenation–acetalization–hydrogenolysis of PHO to CME (Supplementary Fig. 6f–i and Table 1 entries 13–14). In this case, the theoretical maximum yield of CME is only 50% in benzyl phenyl ether and 2-phenylethyl phenyl ether reactions. Different from the reported catalysts (i.e., Pd/C, Ru/HZSM-5, Ni/AlPO₄, Br-Ru/C, Ni-Ru/AC, Ni/Nb₂O₅, and Pd-Ni/AC) showing the hydrogenolysis or overhydrogenation routes with PHO- (e.g., PHO and CHL) + benzene-based derivatives (e.g., benzene and cyclohexane) or dimethyl dicyclohexyl ethers as the main products, Pd/C-O is the first catalyst that can realize the selective preparation of CME from diphenyl ethers, benzyl phenyl ether, and 2-phenylethyl phenyl ether (Supplementary Table 6)^{10,45–50}. In addition, we also demonstrated that CME can be selectively synthesized from *n*-butyl phenyl ether and cyclohexenyl phenyl ether, along with the corresponding alcohols (i.e., *n*-butanol and cyclohexanol, respectively), via the hydrogenation–alcoholysis route (Table 1 entries 15–16). In particular, we were interested in the real bio-oil with various PHO-based monomers (2-methoxy-4-ethyl phenol, 1.3%; 2-methoxy-4-propyl phenol, 10.6%; 2-methoxy-4-propenyl phenol, 1.4%; 2,6-dimethoxy-4-propyl phenol, 21.0%; 4-methyl carboxylate phenol, 2.7%; 2,6-dimethoxy-4-hydroxypropyl phenol, 14.0%; 2-methoxy-4-hydroxypropyl phenol, 7.5%; 2,6-dimethoxy-4-propenyl phenol, 0.9%), obtained via the lignin pyrolysis (Supplementary Fig. 7a)⁵¹. After 12 h, a yield of 41.1% for cyclohexyl ethers was obtained. These results exhibited the excellent universality

of the tandem hydrogenation–acetalization–hydrogenolysis route of phenols and the tandem hydrogenation–alcoholysis–hydrogenation–acetalization–hydrogenolysis route of diphenyl ethers and provide direct access to various cyclohexyl ethers in good to excellent yields.

Identification of hydrogenation sites

As mentioned above, Pd/C cannot catalyze PHO hydrogenation and Pd/C-O showed great catalytic activity, confirming the crucial role of doped O in hydrogenation process. The O content can be readily adjusted from 4.9 wt% to 12.0 wt% by varying the HNO₃ concentration from 5.0 wt% to 20.0 wt% (Supplementary Table 7). Correspondingly, the catalytic activity and selectivity of Pd/C-O were strongly related to its O content, indicating the importance of maximizing the Pd–O–C interface for CME synthesis (Figs. 2c, 3a, Supplementary Fig. 3g, and 7b–d). To investigate the structure–effect relation of these catalysts, the kinetics of PHO hydrogenation, CHO acetalization, and DMC hydrogenolysis were independently assessed. In PHO hydrogenation, it was difficult to obtain the reaction kinetics owing to the inactivation of Pd/C under reaction conditions (110 °C); hence, we focused on the hydrogenation kinetics of Pd/C-O and Ru/C. The hydrogenation kinetics over Ru/C and Pd/C-O followed a pseudo-first-order reaction, as evidenced by the correlation between the PHO conversion rate and reaction time (Supplementary Fig. 7e). Meanwhile, at different PHO concentrations, the initial PHO conversion rate showed a pseudo-first-order reaction order of 0.83–0.88 for PHO (Fig. 3b, Supplementary Fig. 7f–g). Conversely, at different H₂ pressures, the initial PHO conversion rate showed a pseudo-half-order for H₂ (0.43) over Ru/C and a

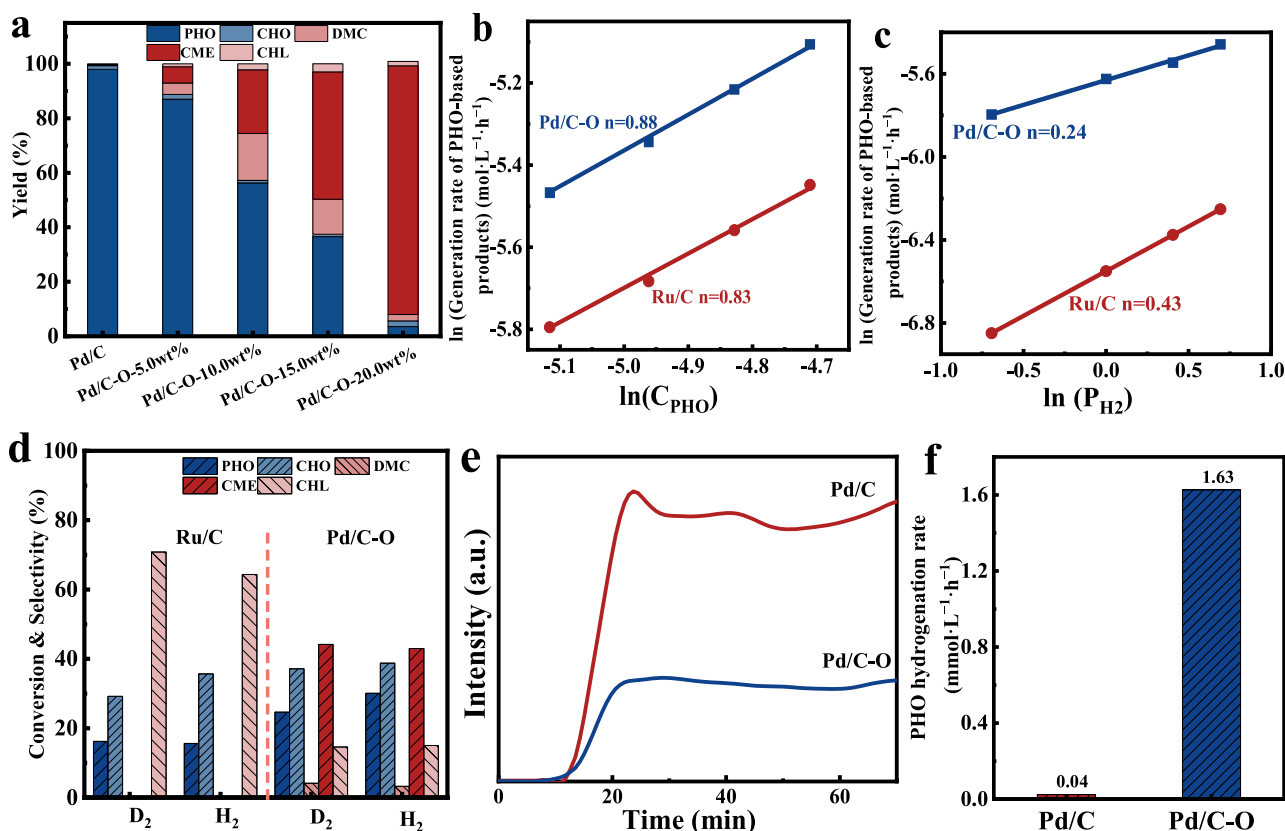


Fig. 3 | Kinetic profiles. **a** Catalytic performance of various catalysts; PHO hydrogenation kinetic experiments over Ru/C and Pd/C-O under different PHO concentrations and **c** H₂ pressure; **d** catalytic performance of PHO reaction over various catalysts under different atmosphere; **e** HD generation signals over Pd/C and Pd/C-O; **f** PHO hydrogenation rate over Pd/C and Pd/C-O. Reaction conditions:

Ru/C (2 mg), Pd/C (20 mg), Pd/C-O (20 mg), methanol (15 mL), temperature (110 °C), **a** PHO (0.09 mmol), H₂ (2.0 MPa), time (6 h); **b** PHO (0.09, 0.105, 0.12, 0.135 mmol), H₂ (2.0 MPa), time (0.5 h); **c** H₂ (0.5, 1.0, 1.5, 2.0 MPa), PHO (0.09 mmol), time (0.5 h); **d** PHO (0.09 mmol), H₂ or D₂ (2.0 MPa), time (0.5 h); **f** PHO (0.09 mmol), H₂ (2.0 MPa), time (0.5 h). The products were quantified by GC.

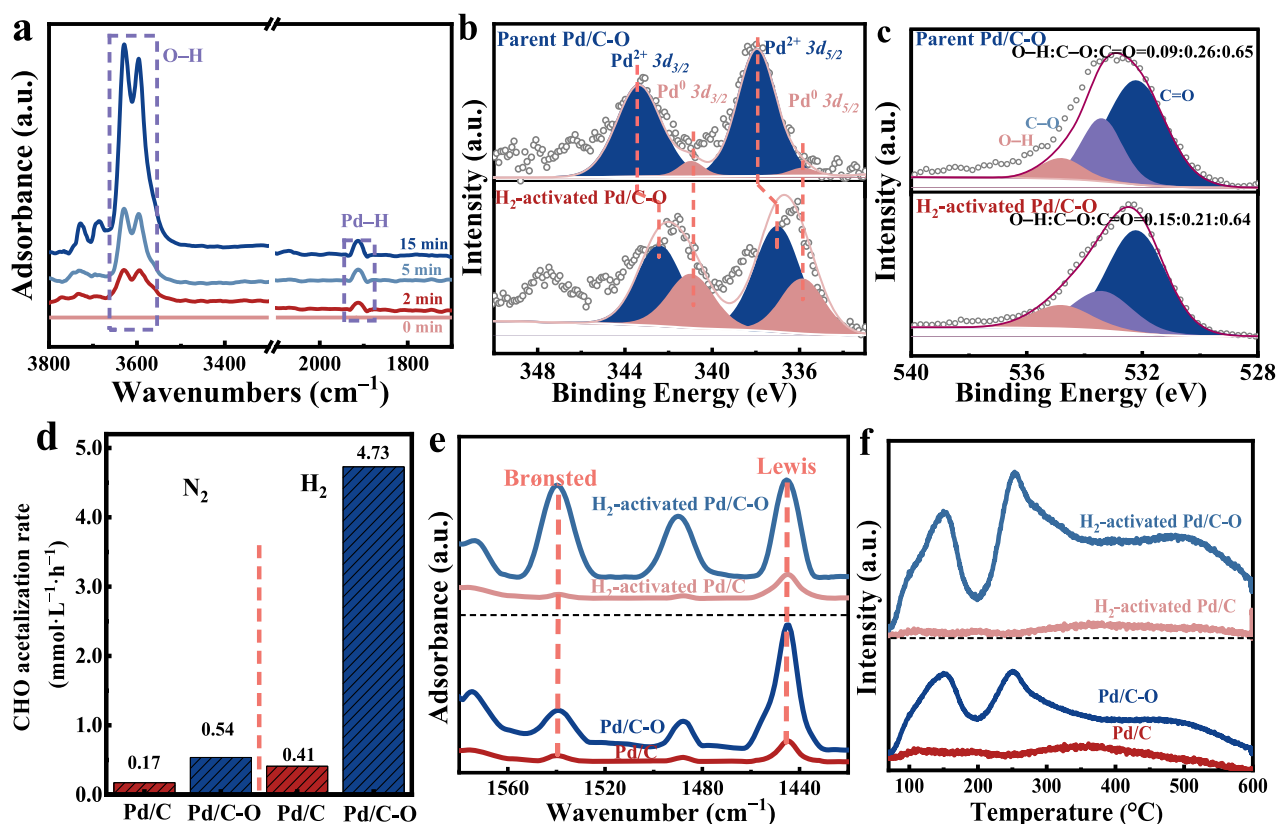


Fig. 4 | Mechanistic study. **a** In situ DRIFT spectra of H_2 -activated Pd/C-O; **b** Pd and **c** O speciation of H_2 -activated Pd/C-O followed by NAP-XPS. **d** CHO acetal rate over Pd/C and Pd/C-O under different atmospheres. Reaction conditions: methanol

(15 mL), reactant (0.09 mmol), temperature (110 °C), catalysts (20 mg), pressure (2.0 MPa), time (0.5 h). **e** Py-FTIR spectra and **f** NH_3 -TPD of Pd/C, Pd/C-O, H_2 -activated Pd/C and H_2 -activated Pd/C-O.

pseudo-zero-order for H_2 (0.24) over Pd/C-O (Fig. 3c, Supplementary Fig. 8a–b). Over Ru/C, hydrogenation exhibited first-order kinetics for PHO and half-order kinetics for H_2 , as expected for a common Langmuir–Hinshelwood mechanism, wherein H_2 and benzene-ring groups were simultaneously adsorbed and saturated at Ru metal sites⁵². Conversely, the unusual first-order kinetics for PHO and zero-order kinetics for H_2 suggested that H_2 was strongly adsorbed and saturated, and the PHO activation step dominated the catalytic process over Pd/C-O (Supplementary Table 8)⁵³. Meanwhile, kinetic isotope tests in a deuterium (D_2) atmosphere exhibited a hydrogenation rate 1.07–1.50 times lower than that in an H_2 atmosphere over Ru/C and Pd/C-O, proving the rapid H_2 activation in PHO hydrogenation over these precious metal catalysts (Fig. 3d)⁵⁴.

Because H_2 activation is an important step for hydrogenation, the H_2 activation ability of these catalysts was thoroughly examined using the H_2 – D_2 exchange test, as indicated by the in situ generated hydrogen deuteride (HD) concentration^{55,56}. At 110 °C, the H_2 activation ability followed the order of Pd/C > Pd/C-O (Fig. 3e). During the H_2 – D_2 exchange test, the amount of water (H_2O) and deuterated water (i.e., HDO and D_2O) cannot be largely detected over Pd/C-O, meaning the O element cannot be leached and has great stability under the reaction conditions (Supplementary Fig. 8c). Interestingly, the initial PHO hydrogenation rate followed the order of Pd/C-O ($1.63 \text{ mol}\cdot\text{L}^{-1}\cdot\text{h}^{-1}$) > Pd/C ($0.04 \text{ mol}\cdot\text{L}^{-1}\cdot\text{h}^{-1}$) (Fig. 3f). Considering the higher hydrogenation rate but the lower H_2 activation ability of Pd/C-O than Pd/C, we hypothesized that Pd sites serve as H_2 activation sites and O sites on the support strongly promote the adsorption and activation of PHO.

The underlying H_2 activation mechanism over Pd/C-O was verified using in situ diffuse reflectance IR FT (DRIFT) spectroscopy. At 110 °C,

upon the introduction of H_2 gas, the intensity of the O–H peak (3547 – 3653 cm^{-1}) strongly increased, accompanied by the appearance of weak Pd–H peak (1893 – 1921 cm^{-1}) (Fig. 4a)^{23,57}. Furthermore, the transformation in the surface chemical structure of Pd/C-O induced by H_2 is further supported by in situ near-ambient-pressure XPS (NAP-XPS) results. The initial NAP-XPS data of Pd/C-O showed Pd $3d$, O $1s$, and C $1s$ signals identical to those observed in the common XPS spectra (Fig. 4b, c and Supplementary Fig. 8d). After the H_2 injection, the Pd $3d$ peaks of Pd^{2+} shifted to lower binding energy ($3d_{5/2}$ peak = 337.0 eV , $3d_{3/2}$ peak = 342.4 eV). Correspondingly, the O $1s$ peaks exhibited a gradual increase in the O–H peak proportion from 0.09 to 0.15, at the expense of the C–O peak, whose proportion decreased from 0.26 to 0.21. Notably, the electronic state of C species remained the same throughout the process (Supplementary Fig. 8d). This observed derivation implied that H_2 underwent homolytic dissociation on Pd nanoparticles and formed H atoms, which migrated to O sites on Pd–O–C. According to the electronegativity order of these atoms ($\text{O} > \text{H} > \text{Pd}$), H atoms on the C–O site afforded O–H⁺ by losing electrons, whereas other H atoms linked to Pd sites formed Pd–H⁺ by accepting electrons^{23,54,58}. The resulting H⁺–O–Pd–H⁺ pair possessed a lower electron density of Pd and a higher electron density of O compared to Pd–O in the parent catalysts. In contrast, the Pd, O, and C species of Pd/C were stable after H_2 activation, which can be ascribed to the low amount of Pd–O–C interfaces (Supplementary Fig. 8e–g). To confirm the hydrogen spillover, tungsten oxide (WO_3) and Pd/C-O were physically mixed in methanol under an H_2 atmosphere²³. The results showed the reduction of the yellow WO_3 into dark blue WO_{3-x} over Pd/C-O, but the color of WO_3 slightly changes over Pd/C (Supplementary Fig. 9a–c). This outcome clearly indicated that the faster hydrogenation rate over Pd/C-O, compared to Pd/C, results from the

in situ generated $\text{H}^+ - \text{H}^-$ pair, ultimately facilitating the adsorption and activation of organic substrates.

Identification of acidic sites

To the best of our knowledge, acidic sites are beneficial for the acetalization of CHO and methanol^{59,60}. The kinetic investigation of CHO acetalization was conducted in a N_2 atmosphere to completely remove the interference of the overhydrogenation route, and the acetalization rate was calculated using the formation rate of DMC. Pd/C and Pd/C-O showed acetalization rates of 0.17–0.54 $\text{mol} \cdot \text{L}^{-1} \cdot \text{h}^{-1}$ (Fig. 4d, Supplementary Fig. 9d–e). In situ pyridine-adsorbed FTIR (Py-FTIR) spectra and temperature-programmed desorption of ammonia (NH_3 -TPD) curves showed a weak adsorbed peak for parent Pd/C (Fig. 4e–f). However, Pd/C-O showed obvious acidity, as indexed by the signals for Lewis (1450 cm^{-1}) and Brønsted acidic sites (1540 cm^{-1}) in Py-FTIR and NH_3 desorption curves at 155, 258, and 497°C . Combined with XPS results, the Lewis and Brønsted acidic sites of Pd/C-O were attributed to Pd^{2+} and OH-containing groups (i.e., $\text{C} = \text{OOH}$ and $\text{C} - \text{OH}$), respectively. The contents of Lewis and Brønsted acidic sites of Pd/C-O were 154.3 and $21.9 \mu\text{mol} \cdot \text{g}^{-1}$, respectively, as calculated from NH_3 -TPD results and the Emeis equation (Supplementary Table 9)^{23,24,58}. In contrast, when the atmosphere was changed to H_2 , the acetalization rate of Pd/C remained almost the same as that in N_2 ($0.41 \text{ mol} \cdot \text{L}^{-1} \cdot \text{h}^{-1}$) but the rate of Pd/C-O increased 8.8-fold compared to that in N_2 ($4.73 \text{ mol} \cdot \text{L}^{-1} \cdot \text{h}^{-1}$), as calculated using the formation rate of the DMC derivatives (DMC and CME) (Supplementary Fig. 9f–h). Correspondingly, after H_2 activation, Pd/C exhibited an acidity similar to its parent counterpart whereas Pd/C-O showed an obvious desorption peak in NH_3 -TPD curves at 258 and 497°C . Meanwhile, the Py-FTIR spectrum of H_2 -activated Pd/C-O showed an enhancement in its Brønsted acidity, accompanied by a decrease in its Lewis acidity. The amounts of Lewis and Brønsted acidic sites changed from 154.3 and 21.9 to 123.6 and $87.3 \mu\text{mol} \cdot \text{g}^{-1}$, respectively (Supplementary Table 9). Similarly, after H_2 activation, Pd/C exhibited a similar basicity to its parent counterpart, as indexed by the temperature-programmed desorption of carbon dioxide (CO_2 -TPD) curves. Whereas Pd/C-O showed an obvious decrease of basicity after H_2 activation, indicating that the conversion of a strong base–weak acid Pd–O–C pair to a strong acid–weak base $\text{H}^+ - \text{Pd} - \text{C} - \text{O} - \text{H}^+$ pair (Supplementary Fig. 10a). Markedly, the acetalization rate was proportional to the amount of in situ generated Brønsted acid.

Furthermore, acidic sites are conducive to the hydrogenolysis reaction as they promote C–O bond activation^{58,61}. Subsequently, the DMC hydrogenolysis step was also evaluated. At different DMC concentrations (0.006–0.009 mol/L), the initial DMC hydrogenolysis conversion rate showed a pseudo-first-order of 0.99–1.01 for DMC over Pd/C and Pd/C-O (Supplementary Fig. 10b). While, at different H_2 pressures (0.5–2.0 MPa), the initial DMC conversion rate showed order of 0.02–0.04 for H_2 over Pd/C and Pd/C-O (Supplementary Fig. 10c). The kinetic results further indicated that H_2 was strongly saturated on the catalyst surface and the adsorption of organic substrate dominates the hydrogenolysis process. The hydrogenolysis rate of Pd/C-O was as high as $4.05 \text{ mol} \cdot \text{L}^{-1} \cdot \text{h}^{-1}$, which exceeded that of Pd/C ($0.49 \text{ mol} \cdot \text{L}^{-1} \cdot \text{h}^{-1}$) by a factor of 8.3 (Fig. 5a, Supplementary Fig. 10d, e). Therefore, the $\text{H}^+ - \text{H}^-$ pair functioned as bifunctional sites, which facilitated PHO hydrogenation and DMC hydrogenolysis steps as asymmetric hydrogenation/hydrogenolysis sites and CHO acetalization step as Brønsted acidic sites.

To distinguish the importance of specific O species ($\text{C} = \text{OOH}$, $\text{C} - \text{OH}$) on the Pd/C-O surface, Pd/C-O-300 was synthesized by the high-temperature N_2 treatment of Pd/C-O to selectively remove $\text{C} = \text{OOH}$ groups⁶². XPS results showed that Pd/C-O-300 possessed a much

weaker signal of $\text{C} = \text{O}$ bond than Pd/C-O but comparable signal intensities of C–O bond and O–H bonds (Supplementary Fig. 11a–c). Pd/C-O-300 showed inferior catalytic activity in the PHO reaction, indicating that the $\text{C} = \text{OOH}$ groups are the key for active sites (Supplementary Fig. 11d–e). To identify whether Brønsted acidic sites were in situ generated $\text{C} = \text{OOH}$ or $\text{C} - \text{OH}$ for the acetalization step, we conducted controlled experiments using a mixture of the Pd/C and liquid organic acids (i.e., benzoic acid and PHO) to catalyze the CHO reaction. The addition of benzoic acid switched the $\text{C} = \text{O}$ hydrogenation route of CHO to the acetalization route over Pd/C (Fig. 5b and Supplementary Fig. 12a). However, PHO did not considerably affect the reaction route because of its well-known relatively weaker acidity than benzoic acid (Supplementary Fig. 12b). This result indicated that the tandem hydrogenation–acetalization–hydrogenolysis route cannot be induced by the self-catalysis of the PHO reactant. Similarly, the DMC generation rate strongly increased with the addition of benzoic acid over Pd/C catalysts (Fig. 5b, Supplementary Fig. 12c, d). Therefore, by tuning the O content of Pd/C and controlling hydrogen spillover, we modulated the hydrogenation–acid catalysis balance and modified the availability of surface $\text{C} = \text{OOH}$ groups for the tandem conversion of PHO to CME.

Understanding the catalytic mechanism

The in situ DRIFT spectra of adsorbed PHO were measured at the reaction temperature (110°C) to investigate the underlying interaction between the catalyst surface and substrate (Fig. 5c). The spectrum of the parent PHO showed peaks at 1495 cm^{-1} (assigned to the $\text{C} = \text{C}$ bond), 1592 cm^{-1} (assigned to the $\text{C} = \text{C}$ bond), 3035 cm^{-1} (assigned to the $\text{C}_{\text{sp}2} - \text{H}$ bond), and 3356 cm^{-1} (assigned to the O–H bond)^{63,64}. In the spectra of Pd/C and Pd/C-O, an additional peak at 2902 cm^{-1} (assigned to the $\text{C}_{\text{sp}3} - \text{H}$ bond) was observed, suggesting that the benzene ring in PHO is horizontally adsorbed and distorted on Pd nanoparticles⁶⁴. After H_2 activation, Pd/C still adsorbed the benzene ring, consistent with the main overhydrogenation route. However, over H_2 -activated Pd/C-O, the signal for $\text{C}_{\text{sp}3} - \text{H}$ cannot be detected but strong signals for $\text{C} = \text{C}$, $\text{C}_{\text{sp}2} - \text{H}$, $\text{C} - \text{O}$, and O–H groups can be detected, indicating that PHO was strongly adsorbed by binding its O atom rather than the benzene ring via a vertical configuration. The strong Brønsted acidic H^+ selectively adsorbed the C–OH group via hydrogen bonding interactions and restrains the attachment of the benzene-ring group. This finding is in agreement with previous studies that reported the promoting effect of Brønsted acidity for PHO adsorption and hydrogenation via OH protonation^{65,66}. Compared with the direct benzene-ring activation route, the C–OH activation route possessed a lower activation energy, considerably enhancing the hydrogenation rate.

To further emphasize the importance of the O atom in the reactant, PHO adsorption experiments were performed using O-free benzene as a reference. Compared with Pd/C-O, Pd/C adsorbed much higher amounts of benzene and PHO (both 20.1% vs. 11.9% and 34.9% vs. 20.2%, respectively), indicating that Pd nanoparticles were conducive to benzene group adsorption (Fig. 5d, e and Supplementary Fig. 12e–h). H_2 -pretreated Pd/C showed adsorption properties similar to those of the parent Pd/C, whereas H_2 -pretreated Pd/C-O adsorbed less benzene (7.2% vs. 11.9%) but more PHO (46.5% vs. 20.2%) than the parent counterpart (Fig. 5d, e and Supplementary Fig. 13a–d). This further indicated the strong interaction of the O–H groups in PHO with the in situ generated $\text{H}^+ - \text{H}^-$ site on the Pd/C-O surface and explained why benzenes (i.e., methylbenzene and ethylbenzene) rather than their further hydrogenated cyclohexanes (i.e., methylcyclohexane and ethylcyclohexane) were formed in diphenyl ether (benzyl phenyl ether and 2-phenylethyl phenyl ether) reactions (Supplementary Fig. 6f–i and Table 1 entries 13–14). The generation of

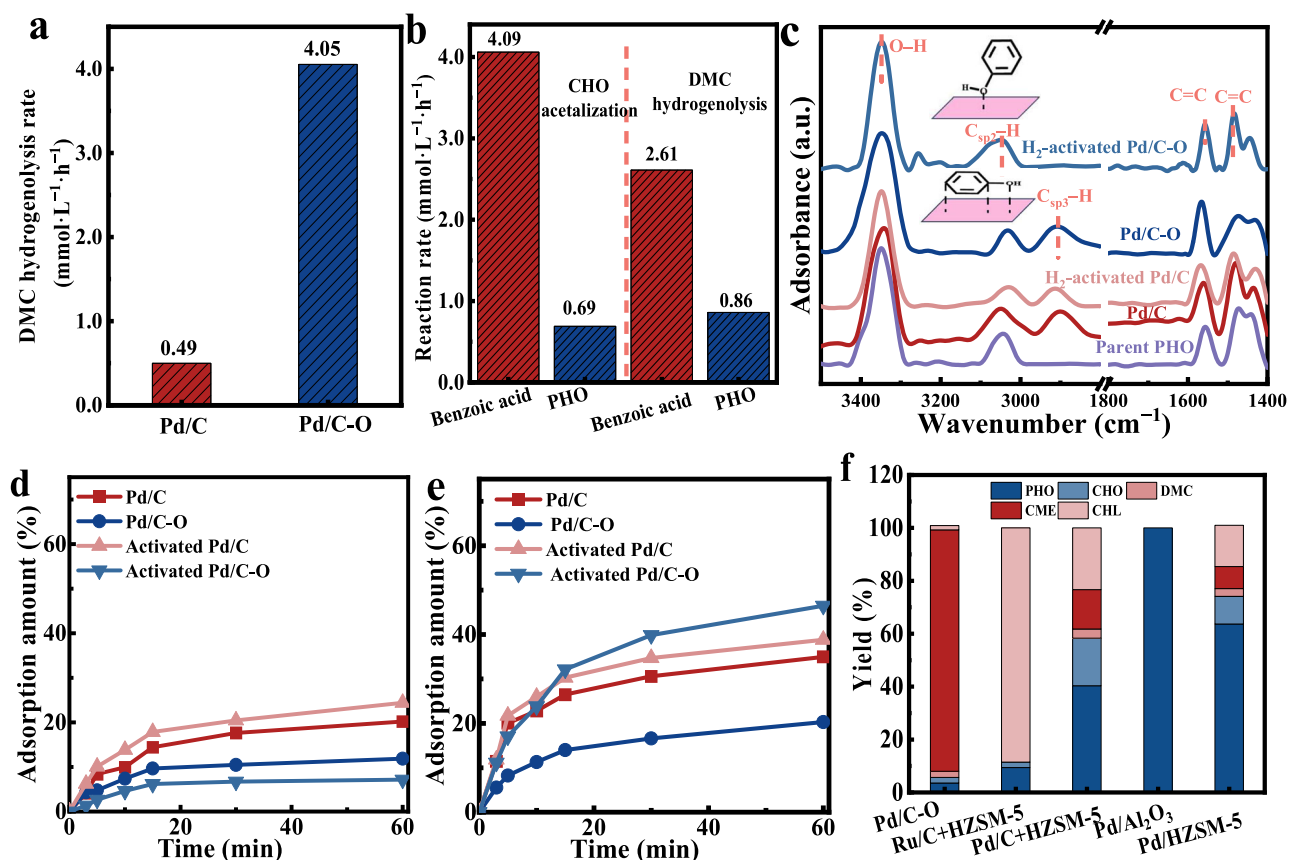


Fig. 5 | Catalytic reactions and adsorption configuration, kinetics over Pd-based Catalysts. a DMC hydrogenolysis rate over Pd/C and Pd/C-O. **b** CHO acetal and DMC hydrogenolysis rate over the mixture of Pd/C and benzoic acid or PHO. **c** in situ DRIFT spectra of adsorbed PHO on various catalysts. The adsorption kinetics of **d** benzene and **e** PHO over different catalysts. Adsorption conditions: methanol (50 mL), catalysts (20 mg), PHO or benzene (0.003 mmol), temperature (30 °C). The concentration was quantified by UV-

visible spectroscopy. **f** The catalytic performance of PHO reaction over the mixture HZSM-5 and Ru/C or Pd/C, Pd/Al₂O₃, Pd/HZSM-5. Reaction conditions: methanol (15 mL), reactant (0.09 mmol), temperature (110 °C), H₂ pressure (2.0 MPa), **a** catalysts (20 mg), time (0.5 h); **b** Pd/C (20 mg), benzoic acid or PHO (0.04 mmol), time (0.5 h); **f** Pd/C-O (20 mg), Pd/Al₂O₃ (20 mg), Pd/HZSM-5 (20 mg), Pd/C (4 mg), or Ru/C (2 mg), HZSM-5 (20 mg), time (6 h). The products were quantified by GC.

H⁺-H⁻ pairs was the premise for PHO adsorption and activation. To investigate the powerful concerted catalysis of the H⁺-H⁻ pairs, a mixture of Brønsted acidic zeolite (HZSM-5) and Ru/C or Pd/C was used for comparison with the same precious metal content and acid amount. Notably, spatially separated hydrogenation sites (Ru/C) and Brønsted acidic sites showed the same catalytic performance as only Ru/C (Fig. 5f and Supplementary Fig. 13e)^{23,67}. Meanwhile, although the mixture of Pd/C and HZSM-5 demonstrated better bifunctional catalytic performance than only Pd/C due to the promotion effect of the Brønsted acid, the PHO conversion and CME selectivity were unsatisfactory (Fig. 5f and Supplementary Fig. 13f)^{65,66}. Similarly, Pd supported acidic supports (such as Pd/Al₂O₃ and Pd/HZSM-5) showed low PHO conversion and CME selectivity owing to the inferior concerted catalysis of metal and acid sites (Fig. 5f, Supplementary Fig. 13g-h). Therefore, the superior performance of such tandem Pd/C-O catalysts resulted from intimate hydrogenation (H⁺-H⁻) and acid sites (H⁺) and short-range diffusion of the CHO intermediate between bifunctional sites facilitated the governed hydrogenation-acetalization-hydrogenolysis route and prevented unwanted overhydrogenation reaction.

Discussion

The Pd/C-O catalyst accelerated the tandem hydrogenation-acetalization-hydrogenolysis of phenol to CME in a methanol solvent

under mild reaction conditions (110 °C). This highly efficient bifunctional catalysis was realized via the in situ generation of H⁺-H⁻ pairs due to the hydrogen spillover from Pd nanoparticles to the Pd-O-C interface. This approach provided unconventional active sites for PHO hydrogenation and DMC hydrogenolysis and also offered acidic sites for CHO acetalization. The prepared catalyst is compatible with various PHO and diphenyl ether substrates and different alcohol solvents with good catalytic performance for cyclohexyl ether synthesis. This study provides a facile and efficient method for tuning the challenging tandem reaction route by oxidizing the catalyst support.

Methods

Preparation of Pd/C-O and Pd/C

Oxygen-doped carbon supported palladium (Pd/C-O) was synthesized by HNO₃ oxidation and subsequent incipient wetness impregnation method. Briefly, 1.0 g of activated carbon and 50 mL of HNO₃ aqueous solution (5.0 wt%, 10.0 wt%, 15.0 wt%, or 20.0 wt%) were mixed and heated to 100 °C for 4 h under stirring. If not mentioned, the HNO₃ concentration was 20.0 wt%. The resultant C-O was obtained by filtration, washing with water until the filtrate became neutral, and subsequently drying under vacuum at 60 °C for 12 h. Then, 0.017 g of PdCl₂ was added to a mixture of 1.0 g of C-O, two drops of dilute hydrochloric acid (2.0 mol·L⁻¹), and 10 mL of ethanol. The mixture were thoroughly mixed at 30 °C. Then, 3 mL of NaBH₄ methanol solution (2.0 mol·L⁻¹) was added to the mixture under vigorous stirring

for 1 h. The Pd/C-O was obtained recovered by filtration and washed with ethanol, and dried at 150 °C for 24 h in a vacuum oven. As a reference, carbon supported palladium (Pd/C) was prepared by the same incipient wetness impregnation method except for the lack of the HNO₃ oxidation step. Pd/C-O-300 was synthesized by the high-temperature N₂ treatment of Pd/C-O at 300 °C for 4 h. Al₂O₃ and HZSM-5 supported palladium (Pd/Al₂O₃, Pd/ZSM-5) were prepared by the same incipient wetness impregnation method.

Characterization methods

Various testing methods, including XRD, ICP-OES, TEM, HR-TEM, EDS analysis, N₂ adsorption-desorption, FTIR, CO pulse purge, Raman, Pd XANES, MS, NH₃-TPD, CO₂-TPD, Py-FTIR, in situ NAP-XPS, and in situ DRIFT spectra were adopted to measure the physicochemical properties and reaction mechanism. The detailed measuring processes are provided in the Supplementary Information.

Catalytic reactions

The synthesis of cyclohexyl ethers was carried out in a 25 mL batch autoclave (Anhui Kemi Instrument Co., LTD.) equipped with a mechanical stirrer. Briefly, 0.09 mmol of phenols or diphenyl ethers, a certain amount of catalyst, and 15 mL of solvent (methanol, ethanol, 2-propanol, and *sec*-butanol) were mixed. If not mentioned, the catalyst amount for phenols and diphenyl ethers was 20 and 50 mg, respectively. Before the reaction, the air in the reactor was replaced with hydrogen several times. Then, the mixture was heated to 110 °C under 2.0 MPa H₂ pressure and periodically sampled with 0.5 mL after reaching the target reaction time. Subsequently, 10 µL of *N,N*-dimethylformamide was used as an internal standard substance. The reaction mixture was qualitatively analyzed by an Agilent 6890 N GC/5973 MS detector and quantitatively analyzed by a Trace 1300 gas chromatograph equipped with a TG-WAXMS capillary column (30 m × 0.32 mm).

Data availability

The source data underlying Figs. 1c–g, 3e, 4a–c, e–f and 5c, and Supplementary Figs. 1a–e, 2b–e, 3a–f, 4d–h, 8c–g, 10a, 11a–c, 12e–h and 13a–d are provided as a Source Data file. All the data that support the findings of this study are available from the corresponding author upon request. Source data are provided with this paper.

References

- Haseeb, S. et al. Conversion of lignin pyrolysis oil to cyclohexyl methyl ethers as a promising biomass-derived solvent. *Green. Chem.* **23**, 2457–2463 (2021).
- Zhang, H. et al. Cyclopentylmethyl ether, a non-fluorinated, weakly solvating and wide temperature solvent for high-performance lithium metal battery. *Angew. Chem. Int. Ed.* **62**, e202300771 (2023).
- Xu, R. et al. Tailoring anion-dominant solvation environment by steric-hindrance effect and competitive coordination for fast charging and stable cycling lithium metal batteries. *J. Energy Chem.* **105**, 35–43 (2025).
- Ravi, S., Mohanavel, V., Dinesh, D. & Anuradha, D. S. Investigational explorations on operation and emission features of C.I engine supplemented by methyl propanol and cyclopentyl ether mixtures. *Mater. Today.: Proc.* **33**, 3297–3302 (2020).
- Luska, K. L., Migowski, P., Sayed, S. E. & Leitner, W. Synergistic interaction within bifunctional ruthenium nanoparticle/SILP catalysts for the selective hydrodeoxygenation of phenols. *Angew. Chem. Int. Ed.* **54**, 15750–15755 (2015).
- Dong, K. et al. Palladium-catalyzed carbonylation of *sec*- and *tert*-alcohols. *Angew. Chem. Int. Ed.* **56**, 6203–6207 (2017).
- Palumbo, C. T. et al. Accessing monomers from lignin through carbon-carbon bond cleavage. *Nat. Rev. Chem.* **8**, 799–816 (2024).
- Liu, W. et al. Ambient-pressure and low-temperature upgrading of lignin bio-oil to hydrocarbons using a hydrogen buffer catalytic system. *Nat. Energy* **5**, 759–767 (2020).
- Liu, H., Jiang, T., Han, B., Liang, S. & Zhou, Y. Selective phenol hydrogenation to cyclohexanone over a dual supported Pd-Lewis acid catalyst. *Science* **326**, 1250–1252 (2009).
- Wu, D. et al. Lignin compounds to monoaromatics: Selective cleavage of C-O bonds over a brominated ruthenium catalyst. *Angew. Chem. Int. Ed.* **60**, 12513–12523 (2021).
- Wang, W. et al. One-step microwave synthesis of micron-sized ZSM-5/MCM-41 hierarchical porous materials for phenol hydroxyl alkylation. *Inorg. Chem. Commun.* **143**, 109738 (2022).
- Chada, R. R. et al. Direct and facile synthesis of LaPO₄ containing SBA-15 catalyst for selective O-methylation of phenol to anisole in continuous process. *Micropor. Mesopor. Mat.* **300**, 110144 (2020).
- Ballarini, N. et al. The transformations involving methanol in the acid- and base-catalyzed gas-phase methylation of phenol. *J. Catal.* **251**, 423–436 (2007).
- Jin, S., Hunt, A. J., Clark, J. H. & McElroy, C. R. Acid-catalysed carboxymethylation, methylation and dehydration of alcohols and phenols with dimethyl carbonate under mild conditions. *Green. Chem.* **18**, 5839–5844 (2016).
- Vriamont, C. E. J. J. et al. From lignin to chemicals: hydro-generation of lignin models and mechanistic insights into hydrodeoxygenation via low temperature C-O bond cleavage. *ACS Catal.* **9**, 2345–2354 (2019).
- He, P. et al. Boosting the catalytic activity and stability of Ru metal clusters in hydrodeoxygenation of guaiacol through MWW zeolite pore constraints. *ACS Catal.* **12**, 14717–14726 (2022).
- Jiang, W. et al. Catalytic hydrogenation of aromatic ring over ruthenium nanoparticles supported on α -Al₂O₃ at room temperature. *Appl. Catal. B: Environ.* **307**, 121137 (2022).
- Tang, H. et al. In situ hydrodeoxygenation of phenol as a model compound for pyrolysis oil using Raney Ni and molecular sieve catalysts. *Energy Fuels* **35**, 4138–4147 (2021).
- He, J., Zhao, C. & Lercher, J. A. Impact of solvent for individual steps of phenol hydrodeoxygenation with Pd/C and HZSM-5 as catalysts. *J. Catal.* **309**, 362–375 (2014).
- Xiang, Y., Ma, L., Lu, C., Zhang, Q. & Li, X. Aqueous system for the improved hydrogenation of phenol and its derivatives. *Green. Chem.* **10**, 939–943 (2008).
- Giannoccaro, P., Gargano, M., Fanizzi, A., Ferragina, C. & Aresta, M. Rh-ions and Rh-complexes intercalated in γ -titanium or γ -zirconium hydrogen phosphate as highly efficient catalysts for arene hydrogenation. *Appl. Catal. A: Gen.* **284**, 77–83 (2005).
- Chen, M. et al. Thermoregulated ionic liquid-stabilizing Ru/CoO nanocomposites for catalytic hydrogenation. *Langmuir* **36**, 11589–11599 (2020).
- Deng, Q. et al. H⁺-H⁻ pairs in partially oxidized MAX phases for bifunctional catalytic conversion of furfurals into linear ketones. *Angew. Chem. Int. Ed.* **62**, e202211461 (2023).
- Deng, Q. et al. Catalytic hydrodehydroxylation of biomass-related chemicals via water-mediated hydrogen heterolysis over a Pd-S interface. *ACS Catal.* **13**, 14356–14366 (2023).
- Das, T. K. et al. Effect of surface functional groups on hydrogen adsorption properties of Pd dispersed reduced graphene oxide. *Int. J. Hydrog. Energy* **42**, 8032–8041 (2017).
- Zhang, P., Wei, J.-S., Chen, X.-B. & Xiong, H.-M. Heteroatom-doped carbon dots based catalysts for oxygen reduction reactions. *J. Colloid Interface Sci.* **537**, 716–724 (2019).
- Herold, F. et al. Synthesis strategies towards amorphous porous carbons with selective oxygen functionalization for the application as reference material. *Carbon* **171**, 658–670 (2021).

28. Navarro-Ruiz, J. et al. Mechanism of hydrogen spillover on metal-doped carbon materials: surface carboxylic groups are key. *ACS Catal.* **14**, 7111–7126 (2024).
29. Machado, B. F. et al. Understanding the surface chemistry of carbon nanotubes: toward a rational design of Ru nanocatalysts. *J. Catal.* **309**, 185–198 (2014).
30. Zhao, Y. et al. Two-step carbothermal welding to access atomically dispersed Pd₁ on three-dimensional zirconia nanonet for direct indole synthesis. *J. Am. Chem. Soc.* **141**, 10590–10594 (2019).
31. Zhang, W. et al. Electrochemical reduction of carbon dioxide to methanol on hierarchical Pd/SnO₂ nanosheets with abundant Pd–O–Sn interfaces. *Angew. Chem. Int. Ed.* **57**, 9475–9479 (2018).
32. Hou, Z. et al. Electronically engineering water resistance in methane combustion with an atomically dispersed tungsten on PdO catalyst. *Angew. Chem. Int. Ed.* **61**, e202201655 (2022).
33. Li, A., Shen, K., Chen, J., Li, Z. & Li, Y. Highly selective hydrogenation of phenol to cyclohexanol over MOF-derived non-noble Co-Ni@NC catalysts. *Chem. Eng. Sci.* **166**, 66–76 (2017).
34. Singh, B. et al. Hydrogenation of lignin-derived feedstocks and bio-oil using active and stable ruthenium catalyst. *Catal. Today* **408**, 139–149 (2023).
35. Feng, G., Liu, Z., Chen, P. & Lou, H. Influence of solvent on upgrading of phenolic compounds in pyrolysis bio-oil. *RSC Adv.* **4**, 49924–49929 (2014).
36. Zhang, X., Du, Y., Jiang, H., Liu, Y. & Chen, R. Insights into the stability of Pd/CN catalyst in liquid phase hydrogenation of phenol to cyclohexanone: role of solvent. *Catal. Lett.* **149**, 3087–3096 (2019).
37. Zhou, H., Wang, H., Sadow, A. D. & Slowing, I. I. Toward hydrogen economy: selective guaiacol hydrogenolysis under ambient hydrogen pressure. *Appl. Catal. B: Environ.* **270**, 118890 (2020).
38. Wu, R. et al. Intermetallic synergy in platinum–cobalt electrocatalysts for selective C–O bond cleavage. *Nat. Catal.* **7**, 702–718 (2024).
39. Zhang, L. et al. Atomically dispersed Co catalyst for efficient hydrodeoxygenation of lignin-derived species and hydrogenation of nitroaromatics. *ACS Catal.* **10**, 8672–8682 (2020).
40. Verma, D. et al. Ga-doped Cu/H-nanozeolite-Y catalyst for selective hydrogenation and hydrodeoxygenation of lignin-derived chemicals. *Green. Chem.* **20**, 3253–3270 (2018).
41. Yan, P. et al. Rh nanoclusters encaged in hollow mesoporous silica nanoreactors with enhanced catalytic performance for phenol selective hydrogenation. *Chem. Eng. J.* **397**, 125484 (2020).
42. Sreenavaya, A., Sahu, A. & Sakthivel, A. Hydrogenation of lignin-derived phenolic compound eugenol over ruthenium-containing nickel hydrotalcite-type materials. *Ind. Eng. Chem. Res.* **59**, 11979–11990 (2020).
43. Xia, H. et al. Tunable selectivity of phenol hydrogenation to cyclohexane or cyclohexanol by a solvent-driven effect over a bifunctional Pd/NaY catalyst. *Catal. Sci. Technol.* **11**, 1881–1887 (2021).
44. Zeng, Y. et al. Highly dispersed Ru nanoparticles anchored on NiAl layered double oxides catalyst for selective hydrodeoxygenation of vanillin. *Catal. Today* **423**, 114252 (2023).
45. Wang, M., Gutiérrez, O. Y., Camaioni, D. M. & Lercher, J. A. Palladium-catalyzed reductive insertion of alcohols into aryl ether bonds. *Angew. Chem. Int. Ed.* **57**, 3747–3751 (2018).
46. Jiang, W. et al. Catalytic hydrodeoxygenation of lignin and its model compounds to hydrocarbon fuels over a metal/acid Ru/HZSM-5 catalyst. *Energy Fuels* **35**, 19543–19552 (2021).
47. Jiang, L., Xu, G. & Fu, Y. Catalytic cleavage of the C–O bond in lignin and lignin-derived aryl ethers over Ni/AlPO₄ catalysts. *ACS Catal.* **12**, 9473–9485 (2022).
48. Zhu, C. et al. Bimetallic effects in the catalytic hydrogenolysis of lignin and its model compounds on Nickel-ruthenium catalysts. *Fuel Process. Tech.* **194**, 106126 (2019).
49. Jiang, W. et al. Selective cleavage of lignin-derived diphenyl ether C–O bond over weakly acidic Ni/Nb₂O₅ catalyst. *Fuel* **295**, 120635 (2021).
50. Xie, J.-X. et al. Catalytic hydrolysis/hydrogenolysis of lignin-derived aryl ethers over bimetallic Pd-Ni systems: the directional regulation of reaction pathways. *ACS Sustain. Chem. Eng.* **11**, 12724–12738 (2023).
51. Shen, Z. et al. Ni₅Fe₅/Al₂O₃ catalytic hydrogenolysis of lignin: mechanism investigation and selectivity regulation. *Green. Chem.* **25**, 7782–7793 (2023).
52. Mohire, S. S. & Yadav, G. D. Selectivity engineering and efficacy of the Ru–Ni@RGO catalyst in hydrogenation of *p*-tert-butylphenol to *p*-tert-butylcyclohexanol. *Ind. Eng. Chem. Res.* **62**, 19524–19535 (2023).
53. Chen, S. et al. Increased hydrogenation rates in Pd/La–Al₂O₃ catalysts by hydrogen transfer O(–La) sites adjacent to Pd nanoparticles. *ACS Catal.* **12**, 15696–15706 (2022).
54. Liu, P. et al. Photochemical route for synthesizing atomically dispersed palladium catalysts. *Science* **352**, 797–800 (2016).
55. Gao, R. et al. Pd/Fe₂O₃ with electronic coupling single-site PdFe pair sites for low-temperature semihydrogenation of alkynes. *J. Am. Chem. Soc.* **144**, 573–581 (2022).
56. Drescher, T., Niefind, F., Bensch, W. & Grünert, W. Sulfide catalysis without coordinatively unsaturated sites: hydrogenation, cis-trans isomerization, and H₂/D₂ scrambling over MoS₂ and WS₂. *J. Am. Chem. Soc.* **134**, 18896–18899 (2012).
57. Yang, D. et al. Co-catalysis over a bi-functional ligand-based Pd-catalyst for tandem bis-alkoxycarbonylation of terminal alkynes. *Green. Chem.* **20**, 2588–2595 (2018).
58. Ouyang, Z. et al. Palladium single atom-supported covalent organic frameworks for aqueous-phase hydrogenative hydrogenolysis of aromatic aldehydes via hydrogen heterolysis. *Angew. Chem. Int. Ed.* **64**, e202418790 (2024).
59. Iwamoto, M., Tanaka, Y., Sawamura, N. & Namba, S. Remarkable effect of pore size on the catalytic activity of mesoporous silica for the acetalization of cyclohexanone with methanol. *J. Am. Chem. Soc.* **125**, 13032–13033 (2003).
60. Bailey, L. A., Bere, T., Davies, T. E., Taylor, S. H. & Graham, A. E. Preparation of biomass-derived furfuryl acetals by transacetalization reactions catalyzed by nanoporous aluminosilicates. *ACS Sustain. Chem. Eng.* **10**, 13759–13764 (2022).
61. Deng, Q. et al. 2D MOF with compact catalytic sites for the one-pot synthesis of 2,5-dimethylfuran from saccharides via tandem catalysis. *Angew. Chem. Int. Ed.* **61**, e202205453 (2022).
62. Dang, Y. et al. Carbon surface chemistry: benchmark for the analysis of oxygen functionalities on carbon materials. *Adv. Mater.* **37**, 2418239 (2025).
63. Zhu, L. et al. Tartaric acid-assisted synthesis of well-dispersed Ni nanoparticles supported on hydroxyapatite for efficient phenol hydrogenation. *ACS Sustain. Chem. Eng.* **10**, 10526–10536 (2022).
64. de Souza, P. M. et al. Role of keto intermediates in the hydrodeoxygenation of phenol over Pd on oxophilic supports. *ACS Catal.* **5**, 1318–1329 (2015).
65. Nelson, N. C., Manzano, J. S., Sadow, A. D., Overbury, S. H. & Slowing, I. I. Selective hydrogenation of phenol catalyzed by palladium on high surface-area ceria at room temperature and ambient pressure. *ACS Catal.* **5**, 20512061 (2015).
66. Jin, X. et al. Metal-support cooperation in Al(PO₃)₃-supported platinum nanoparticles for the selective hydrogenolysis of phenols to arenes. *Nat. Catal.* **4**, 312–321 (2021).
67. Jin, Z. et al. Metal-acid interfaces enveloped in zeolite crystals for cascade biomass hydrodeoxygenation. *Appl. Catal. B: Environ.* **254**, 560–568 (2019).

Acknowledgements

We appreciate the supports from the National Natural Science Foundation of China (22178158, 52162014, 22308135), the Outstanding Youth Science Fund Project of Jiangxi Province (20224ACB213008), the Jiangxi Provincial Double Thousand Talents Plan-Youth Program (S2021GDQN0947), Key project of Jiangxi Provincial Natural Science Foundation (20242BAB26039), Jiangxi Provincial Natural Science Foundation (20224BAB213023, 20232BAB203055), and the Gan Po Brilliant Support Program-Young Science and Technology Talent Assist Project (2024QT09).

Author contributions

L.J. and X.L.: preparation and characterization of catalysts. Y.M., Y.H., Y.P., and M.M.: performing the catalytic reactions. C.S.: synthesis of real bio-oil. J.W., J.-J.Z., and Q.D.: overall direction of the project. Q.D. wrote the manuscript with the help from all authors.

Competing interests

The authors declare no competing interests.

Additional information

Supplementary information The online version contains supplementary material available at <https://doi.org/10.1038/s41467-025-60268-5>.

Correspondence and requests for materials should be addressed to Qiang Deng.

Peer review information *Nature Communications* thanks Jing-Pei Cao, Mathew Rasmussen and the other, anonymous, reviewer(s) for their

contribution to the peer review of this work. A peer review file is available.

Reprints and permissions information is available at <http://www.nature.com/reprints>

Publisher's note Springer Nature remains neutral with regard to jurisdictional claims in published maps and institutional affiliations.

Open Access This article is licensed under a Creative Commons Attribution-NonCommercial-NoDerivatives 4.0 International License, which permits any non-commercial use, sharing, distribution and reproduction in any medium or format, as long as you give appropriate credit to the original author(s) and the source, provide a link to the Creative Commons licence, and indicate if you modified the licensed material. You do not have permission under this licence to share adapted material derived from this article or parts of it. The images or other third party material in this article are included in the article's Creative Commons licence, unless indicated otherwise in a credit line to the material. If material is not included in the article's Creative Commons licence and your intended use is not permitted by statutory regulation or exceeds the permitted use, you will need to obtain permission directly from the copyright holder. To view a copy of this licence, visit <http://creativecommons.org/licenses/by-nc-nd/4.0/>.

© The Author(s) 2025